Array effects in electromagnetic surveying: misplacement of anomaly locations in 1D inversion

Jian Chen[1], Frans Schaars[2], Gianluca Fiandaca[1]

[1]The EEM Team for Hydro & eXploration, Department of Earth Sciences "Ardito Desio", University of Milano, Via Botticelli 23, Milano (Italy).

[2]Artesia, the Netherlands.

Corresponding author: Jian Chen (jian.chen@unimi.it)

Summary

Laterally distributed conductive bodies and intervening resistive regions within the transient electromagnetic (TEM) sensitivity region can produce anomalously enhanced responses over resistive zones. When interpreted with standard one-dimensional (1D) inversion, this response pattern can lead to laterally misplaced conductive anomalies. We refer to this family of inversion artefacts as array effects, because they arise when a subsurface array of conductive and resistive features jointly contributes to the measured TEM response, causing 1D inversion to recover conductive anomalies at incorrect lateral positions. The underlying physical cause is the conductive–resistive alternation mechanism: spatially separated conductive regions, interleaved with resistive gaps, can jointly influence the measured response, causing 1D inversion to place conductive anomalies into, or towards, intervening resistive regions. This produces severe artefacts in inversion models and can mislead geological interpretation. Such conditions may occur in geological settings characterized by repeated lateral electrical heterogeneity, provided that the electrical contrast and spacing are appropriate. Using smoke-ring theory and 3D numerical modelling, we investigate how these effects arise and propose the Instantaneous Smoke Ring Footprint (InSR-Footprint) as a practical criterion for model design and effect identification. Finally, we present field evidence for array effects in SkyTEM data acquired over a coastal dune environment in the Netherlands.

Key words: Electromagnetic theory, Inverse theory, Numerical modelling, Numerical approximations and analysis.

1 Introduction

The transient electromagnetic method (TEM) is a geophysical technique that images subsurface electrical structure by measuring the decay of secondary fields generated by induced eddy currents. Thanks to the rapid development of ground-based TEM systems (Auken et al., 2019), airborne TEM systems such as SkyTEM (Sørensen & Auken, 2004), Geotech's VTEM system (Witherly et al., 2004), and TEMPEST (Lane et al., 2000), as well as waterborne TEM systems (Lane Jr et al., 2020), TEM technology has been widely applied in fields including hydrogeological exploration (Viezzoli et al., 2010; Silvestri et al., 2019; Chandra et al., 2021; Chen et al., 2025) and mineral resource prospecting (González-Álvarez et al., 2015; Macnae & Hine, 2025; Zhdanov et al., 2025).

TEM data inversion is the process of finding a geoelectric model whose simulated responses can fit the observed data (Ellis, 1998). The most extensively applied inversion method is grounded in the assumption of a layered earth model, termed one-dimensional (1D) inversion. This approach presupposes that geoelectric parameters vary exclusively with depth and exhibit horizontal homogeneity. The response at each measurement point can be reproduced by assigning electrical parameters to a multi-layered model beneath it. Subsequently, all survey data are interpreted using a stitched 1D model, which can be further optimized by imposing smoothness or sharpness constraints (Vignoli et al., 2015; Lin et al., 2021; Chen et al., 2023). Auken et al. (2008) established that the 1D inversion algorithm incorporating smoothness constraints can effectively attenuate the impact of three-dimensional (3D) effects and data noise through the diffusion of information from adjacent measurement points. Additionally, as the constraint strength can be modulated to accommodate regional geological variability, this smooth inversion is also suitable for geological environments exhibiting moderate two-dimensional (2D) and 3D variations (Viezzoli et al., 2008).

Over the past two decades, advancements in computer performance have made significant progress in 2.5-dimensional (2.5D) and 3D inversion methods based on Maxwell's equations. Currently, various methods are available for 3D forward modelling, including the finite difference method (Commer and Newman

2004), finite element method (Yin et al., 2016), finite volume method (Haber et al., 2007), and integral equation method (Cox et al., 2010). Innovative techniques such as moving footprint (Cox et al., 2010), decoupling model and forward mesh (Zhang et al., 2021), and local mesh (Haber and Schwarzbach 2014; Yang et al., 2014) have significantly enhanced the practicality of 3D inversion. Moreover, driven by the growing demand for mineral resource exploration, 3D inversion has gradually evolved from inverting only resistivity parameters to incorporating induced polarization parameters (Cox et al., 2024; Chen et al., 2026a). Despite considerable advancements, 3D inversion still faces efficiency limitations compared to 1D inversion when processing large-scale datasets. As a result, 1D methods have long been the industry standard for interpreting TEM data. This prompts an essential question: how much does 1D inversion fail when dealing with 2D or 3D structures?

Ellis (1998) investigated the applicability of 1D inversion in multidimensional geological environments. His results indicated that 1D inversion could well recover the local features of the real anomaly layer, but distortions would occur near the edges of the anomaly. He also pointed out that the data misfit of 1D inversion could not serve as an indicator to assess the existence of 3D effects. Ley-Cooper et al. (2010) demonstrate that in electrically conductive environments, large-scale subhorizontal conductors, such as those formed by saline water or clay layers, can be effectively detected by airborne electromagnetic methods (AEM) and well reconstructed through 1D inversion. Moreover, their conclusions indicate that when eroded paleochannel structures or subvertical geological boundaries are present, 1D inversion may inaccurately infer the presence of a weak conductor at depth within a resistive hole. Yang and Oldenburg (2012) demonstrated that when a strong 3D geometric structure exists in an underground deposit, 1D inversion can produce severe artefacts. For instance, it may incorrectly image a high-resistivity rock mass surrounded by conductors (e.g. the sedimentary model of Mt. Milligan in Canada) as a conductor. Cox et al. (2012) contended that 1D inversion generates artefacts in terrains characterized by laterally varying conductive geological features. These artefacts typically manifest as conductive features at depth, potentially masking higher-resistivity basements and deeper conductors. Silic et al. (2018) compared the differences between

1D and 2.5D inversion methods. They simulated an off-end effect, where anomalies in the leading edge of the overall response are recorded as the observation system approaches a large conductor but has not yet reached it. In such cases, 1D inversion generates an independent “ghost” conductor. The study by Paterson (2020) showed that the 1D method is only relatively accurate when the dip angle of the strata is less than about 20° without significant lateral conductivity. In steeply dipped and complex geological structures, the 1D inversion results are prone to showing conductivity characteristics at incorrect depths. For example, syncline geological structures may be interpreted as anticlines by the 1D method. Oldenburg et al. (2019) demonstrated through simulations of the 2D response of a vertical conductor that a 1D inversion would produce a trouser leg-shaped anomaly for an isolated conductor. This phenomenon arises because the detection system can sense the presence of a large conductive anomaly even when it is not directly above it. As a result, the 1D method generates a drooping trouser leg anomaly at both ends of the conductive body. Recently, Heagy et al. (2025) demonstrated the importance of performing additional 3D forward simulation following standard 1D inversion to assess the reliability of the results.

The aforementioned studies highlight a broad consensus: where multidimensional effects are present, 1D inversion results may produce misleading artefacts. However, the research presented in this paper shows that lateral variations in subsurface conductivity can have a more severe influence on 1D inversion than previously acknowledged, causing conductive anomalies to be misplaced into, or towards, resistive regions. We refer to this family of 1D inversion artefacts as array effects. Here, “array” refers to a spatial arrangement of conductive and resistive features within the effective TEM response region, rather than to the acquisition geometry. The underlying physical cause is the conductive–resistive alternation mechanism: spatially separated conductive regions and intervening resistive regions can jointly contribute to the measured TEM response, causing 1D inversion to recover conductive anomalies at incorrect lateral positions. Importantly, these misplacements may occur even when the 1D inversion fits the data well; therefore, data misfit is not a reliable indicator of the spatial accuracy of the recovered model. By integrating Nabighian’s (1979) smoke-ring theory with 3D forward modelling, we analyse the conductive–resistive alternation mechanism, develop a strategy for modelling and identifying array effects, and present supporting field evidence using SkyTEM data acquired in the Netherlands.

2. Array effects

2.1 Array effects and the conductive–resistive alternation mechanism

In the TEM method, after the transmitter current is turned off, the induced eddy currents in the subsurface exhibit a 'smoke ring effect,' diffusing both downward and outward as the delay time increases (Nabighian, 1979). Figure 1(a) shows the current density distribution calculated using a semi-analytical solution based on Ward and Hohmann (1988), with Stehfest's algorithm used for the numerical inverse Laplace transform. The trajectory of the maximum current density diffuses downward at an angle of approximately 28° relative to the surface, consistent with the results of Hoversten and Morrison (1982). Consequently, the effective investigation zone of TEM can be approximated as a dynamically expanding region. In a 2D section, this region has a trapezoidal character: its upper width is mainly controlled by the transmitter-loop size, whereas its lower width is governed by observation time and subsurface conductivity.

The physical mechanism considered in this study is referred to here as the conductive–resistive alternation mechanism, because it arises from the joint TEM response of spatially separated conductive bodies and intervening resistive regions. Taking a 2D scenario as an example, assume that two adjacent conductive anomalies occur at a similar depth and are separated by a resistive gap. At a given delay time, the core influence zone of the induced current can be approximated as a rectangle that expands with time and migrates downward. When the observation system is positioned above the resistive gap between the two anomalies, this influence zone may cover both conductive bodies simultaneously. The two bodies are then jointly energized, producing a superimposed secondary-field response. Conversely, when the system is positioned directly above one conductive body, the influence zone may not cover the neighbouring conductor to the same extent, and the total response can be weaker than that observed above the intervening resistive gap (Figure 1b). In 1D inversion, this non-local response may be interpreted as a local conductive feature beneath the observation point, producing a spurious conductive anomaly within the resistive gap between the true conductors.

We use the term array effects for this family of 1D inversion artefacts. In this context, “array” refers to a spatial arrangement of conductive and resistive subsurface features within the effective TEM response region, not to the transmitter, receiver, or survey geometry. This definition includes both quasi-2D arrangements, where conductive and resistive features vary mainly along one horizontal direction, and fully 3D arrangements, where such features vary in two horizontal directions. In both cases, the physical cause is the same conductive–resistive alternation mechanism: spatially separated conductive regions, interleaved with resistive gaps or resistive cells, can jointly contribute to the measured TEM response, causing 1D inversion to misplace conductive anomalies into, or towards, intervening resistive regions. Such misplaced conductive anomalies can severely distort 1D inversion models and mislead geological interpretation and decision-making.

The geological relevance of such conductive–resistive arrangements depends primarily on electrical contrast and spatial scale. Some geological settings may produce repeated lateral segmentation or alternating conductive and resistive zones at scales relevant to TEM investigation. Examples may include 2D or quasi-2D settings such as sand dunes, ripples, moraines, karst terrains, horst-and-graben structures, and mineralized vein systems (Moon, 2010), as well as more complex 3D settings such as spheroidal weathering. These examples should be regarded as potential settings only; their relevance depends on whether they produce sufficient electrical contrast and length scales to couple multiple conductive regions and intervening resistive regions within the instantaneous TEM influence zone.

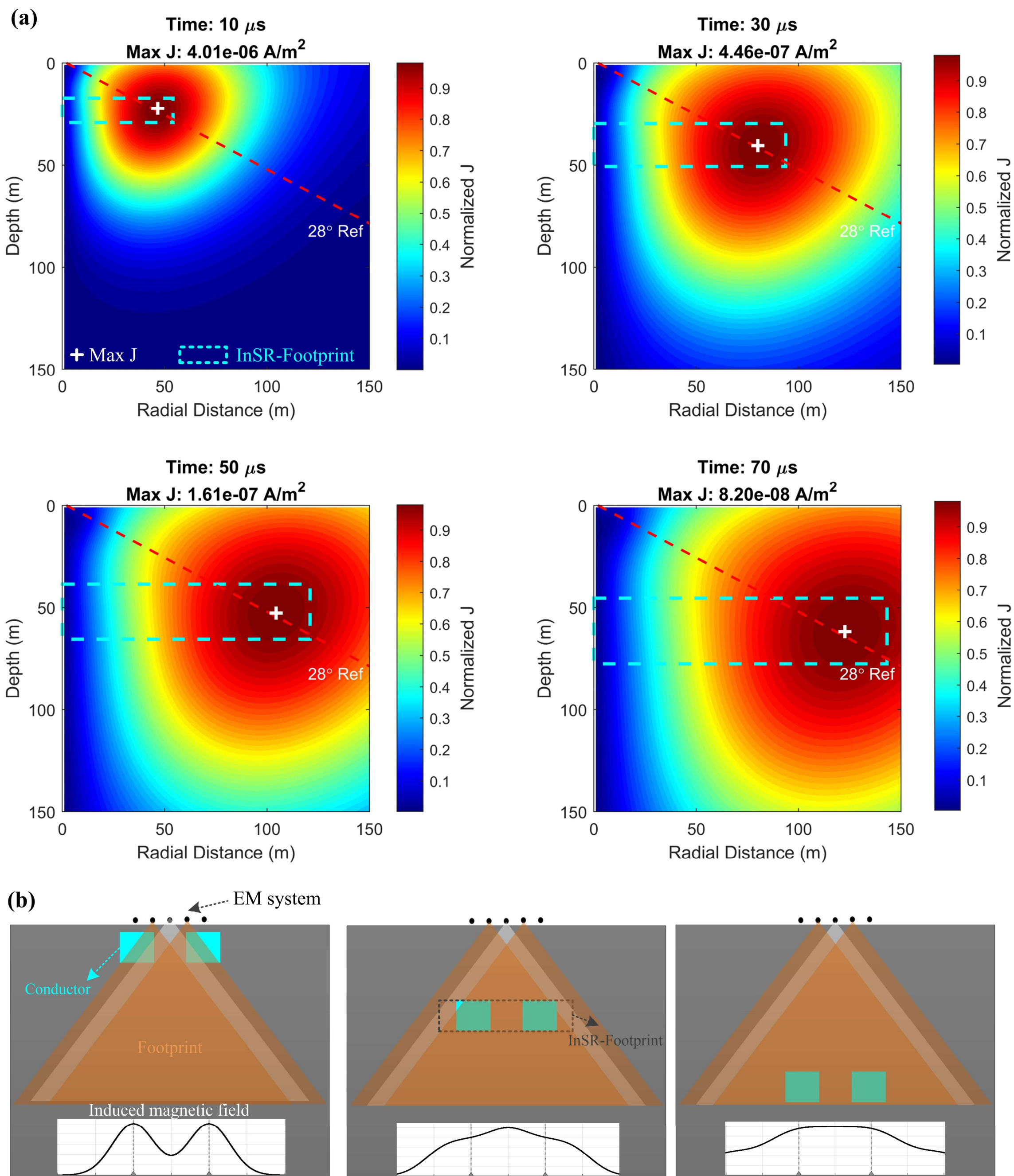

Figure 1. Conceptual basis of the conductive–resistive alternation mechanism and the InSR-Footprint. (a) Normalized current-density distribution in the right half-plane for a homogeneous half-space model (loop radius $a = 2$ m, resistivity $\rho = 100\ \Omega \cdot$ m), shown as a function of delay time, depth, and radial distance. The red dashed line marks the 28° smoke-ring reference trajectory, and the cyan dashed rectangle outlines the Instantaneous Smoke Ring Footprint (InSR-Footprint). (b) Schematic illustration of how conductive bodies separated by resistive gaps interact with the TEM influence zone, illustrating the conductive–resistive alternation mechanism responsible for array effects in 1D inversion.

As shown in Figure 1(b), the occurrence of array effects is controlled by the relationship between the spatial distribution of conductive bodies, intervening resistive regions, and the instantaneous influence zone of the TEM response. To quantify this relationship and guide the modelling of array effects, we define the core region of the instantaneous current density as the Instantaneous Smoke Ring Footprint (InSR-Footprint). This concept differs fundamentally from the conventional 'electromagnetic footprint.' While the conventional term refers to the subsurface sensitivity integrated over the entire time domain, the InSR-Footprint isolates the spatial distribution of the eddy current ring at a specific instant or depth. Numerically, this is defined using a threshold: the InSR-Footprint corresponds to the prism enclosing normalized current density values exceeding 0.95. In a homogeneous half-space, based on the vertical velocity of the diffusing 'smoke ring' current derived by Nabighian (1979), the diffusion depth (δ) of the 'smoke ring' centre at time t satisfies:

$$\delta(t) = \sqrt{4t/\pi\mu_0\sigma} \quad (1)$$

where σ is the subsurface conductivity, and μ_0 is the permeability of free space. This diffusion depth does not correspond to the depth of maximum normalized current, but is a fraction of it, as detailed below.

The dimensions (length and vertical boundaries) of the InSR-Footprint, as defined in this study, were estimated by analyzing the current density distribution using the semi-analytical solution of Ward and Hohmann (1988). Numerical experiments demonstrate that these dimensions can be expressed as linear functions of the diffusion depth (Equation 1). Specifically, our findings can be summarized as follows:

$$L_{InSR}(t)/2 = \sqrt{(C_h \cdot h)^2 + a^2} + C_L \cdot \delta(t) \quad (2)$$

$$Z_{top}(t) = C_{zt} \cdot \delta(t) \quad (3)$$

$$Z_{bot}(t) = C_{zb} \cdot \delta(t) \quad (4)$$

where $L_{InSR}(t)$ is the length of the rectangular InSR-Footprint at time t, h is the height of the transmitter loop above the ground, a is the radius of the transmitter loop, C_L is a coefficient for radial diffusion, and C_h is a coefficient for mapping the air-layer height. Additionally, Z_{top} and Z_{bot} represent the depths of the top and bottom boundaries of the rectangle, respectively, with C_{zt} and C_{zb} serving as their respective vertical diffusion coefficients.

In this paper, the empirical coefficients of Equations 2, 3 and 4 retrieved through numerical modelling are: $C_L = 1.70$, $C_{zt} = 0.54$ and $C_{zb} = 0.92$. As illustrated by the blue dashed rectangle in Figure 1(a), the InSR-Footprint calculated with these parameters effectively encapsulates the core region of maximum current density.

However, the depth of maximum current density (indicated by the white '+' marker in Figure 1(a)) represents only a fraction of the diffusion depth. Notably, the diffusion depth calculated using the smoke ring trajectory formula (Equation 1) tends to slightly overestimate the depth relative to the semi-analytical solution (Oristaglio & Hohmann, 1984). This behaviour is consistent with our findings, which locate the geometric centre of the InSR-Footprint at approximately 0.73 times the smoke ring diffusion depth (calculated as the average of 0.54 and 0.92).

Finally, the C_h coefficient in Equation (2) accounts for the air layer between the transmitter and the ground, which is essential for modelling the flight height of AEM systems. This height-mapping coefficient projects the airborne loop onto an equivalent ground radius. Following the footprint concept of Liu and Becker (1990), in which the lateral scale of an AEM footprint is related to flight height, we use 3.7 times the flight height as an empirical estimate of the equivalent ground side length. For the circular-loop configuration used in this study, this gives a corresponding $C_h$value of 2.1 $\left(C_h = \sqrt{3.7^2/\pi}\right)$. This coefficient is used here as an empirical height-mapping term for the central-loop/small-offset loop configuration considered in our modelling.

The relevant scale for array effects is not the absolute width of an individual resistive region alone, but its size relative to the InSR-Footprint. A necessary condition is that at least two conductive bodies and the intervening resistive region occur within the same InSR-Footprint. If the resistive region is much smaller than the effective lateral resolution, the adjacent conductors are sensed approximately as a single conductive body. If the resistive region is much larger than the InSR-Footprint, the conductors are sensed independently and the misplacement effect is reduced. Thus, array effects are expected to be most pronounced when adjacent conductive bodies remain electromagnetically coupled across a resolvable resistive region within the same InSR-Footprint. This criterion is most directly applicable to central-loop TEM/AEM or other small-offset systems similar to those modelled here. Systems with larger transmitter–receiver offsets, especially fixed-transmitter configurations, may have substantially different sensitivity patterns; therefore, the equivalent InSR-Footprint and corresponding scale criterion would need to be redefined or recalibrated.

For instance, considering a ground-based TEM system with a loop radius of 2 m, a target centre depth of 35 m corresponds to a smoke-ring diffusion depth of approximately 48 m. Calculations using Equations (2)–(4) show that, at this depth, the InSR-Footprint spans a vertical range from 26 m to 44 m and has a horizontal length of approximately 167 m. For the synthetic models in the next section, the widths of both the conductive bodies and the intervening resistive gaps are set to approximately one-quarter of this InSR-Footprint length, following the conceptual scheme in Figure 1(b). This scaling is sufficient to couple adjacent conductive bodies and intervening resistive gaps within the same InSR-Footprint. As shown in the next section, this configuration produces ghost conductive anomalies in 1D inversion that resemble the true anomalies in lateral extent but appear at incorrect lateral positions, commonly within or towards the intervening resistive regions.

2.2 2D and 3D synthetic modelling

Building upon the empirical formulas derived in the preceding section, this section uses synthetic simulations to investigate array effects in 2D and 3D conductive–resistive array models. Since accurate representation of these effects requires full 3D physics, 3D forward modelling is necessary. This paper adopts a 3D TEM forward modelling algorithm based on the vector finite element method, developed on the EEMverter software platform (Fiandaca et al., 2024). For details regarding the algorithm and its accuracy verification, please refer to Chen et al. (2026a). After generating synthetic data using the 3D code, to isolate the influence of multidimensional effects on the anomaly distribution recovered during inversion, no noise was introduced into the data. Each datum was assigned a standard deviation of 3% for the inversion. The 1D and 3D inversions were conducted using the Levenberg-Marquardt linearized approach for iterative optimization. Apart from the differences in forward-modelling kernels, all other inversion parameters remained consistent between the 1D and 3D inversion processes.

First, we constructed a 2D conductive–resistive array model tailored to the specifications of the ground-towed transient electromagnetic (tTEM) system. This model represents a single row of alternating conductive bodies and resistive regions. The background resistivity was set to 100 Ω·m, while the conductive bodies were assigned a value of 20 Ω·m. Based on the calculations in Section 2.1, anomalies centred at a depth of 35 m correspond to an InSR-Footprint horizontal length of approximately 167 m and a vertical depth range of 26–44 m. Informed by these parameters, the conductive bodies were designed with an XZ cross-section of 40 m × 12 m. As illustrated in Figure 2(a), this model comprises eight conductive bodies spaced 40 m apart within the 30–42 m depth interval. Furthermore, we developed a deep-target 2D array model centred at 80 m. At this depth, the InSR-Footprint corresponds to a length of ~370 m and a vertical span of 60–100 m. Accordingly, as shown in Figure 2(b), three large conductive anomalies with a thickness of ~40 m and a spacing of 90 m were incorporated. Figure 2(c) depicts the corresponding 3D conductive–resistive array model, reflecting the same burial depths as in Figure 2(a), but with conductive and resistive cells alternating in two horizontal directions. For both the 2D and 3D simulations, the tTEM line and sounding spacings were fixed at 10 m.

The right side of Figure 2 displays the 1D inversion results corresponding to these conductive–resistive array models, while the 3D inversion results are shown in Figure 3. For the 3D array model, the 1D inversion recovers a laterally alternating conductive pattern, but the positions of the conductive features are strongly misplaced, with conductive anomalies appearing mainly over the resistive cells. In contrast, the 3D inversion recovers the conductor distribution much more accurately. A similar phenomenon is observed in the 2D array models. In Case A, the 1D inversion recovers seven strongly conductive anomalies, but their positions are almost completely offset from the true conductor locations. Similarly, in Case B, the 1D inversion places the most conductive anomaly within a high-resistivity zone.

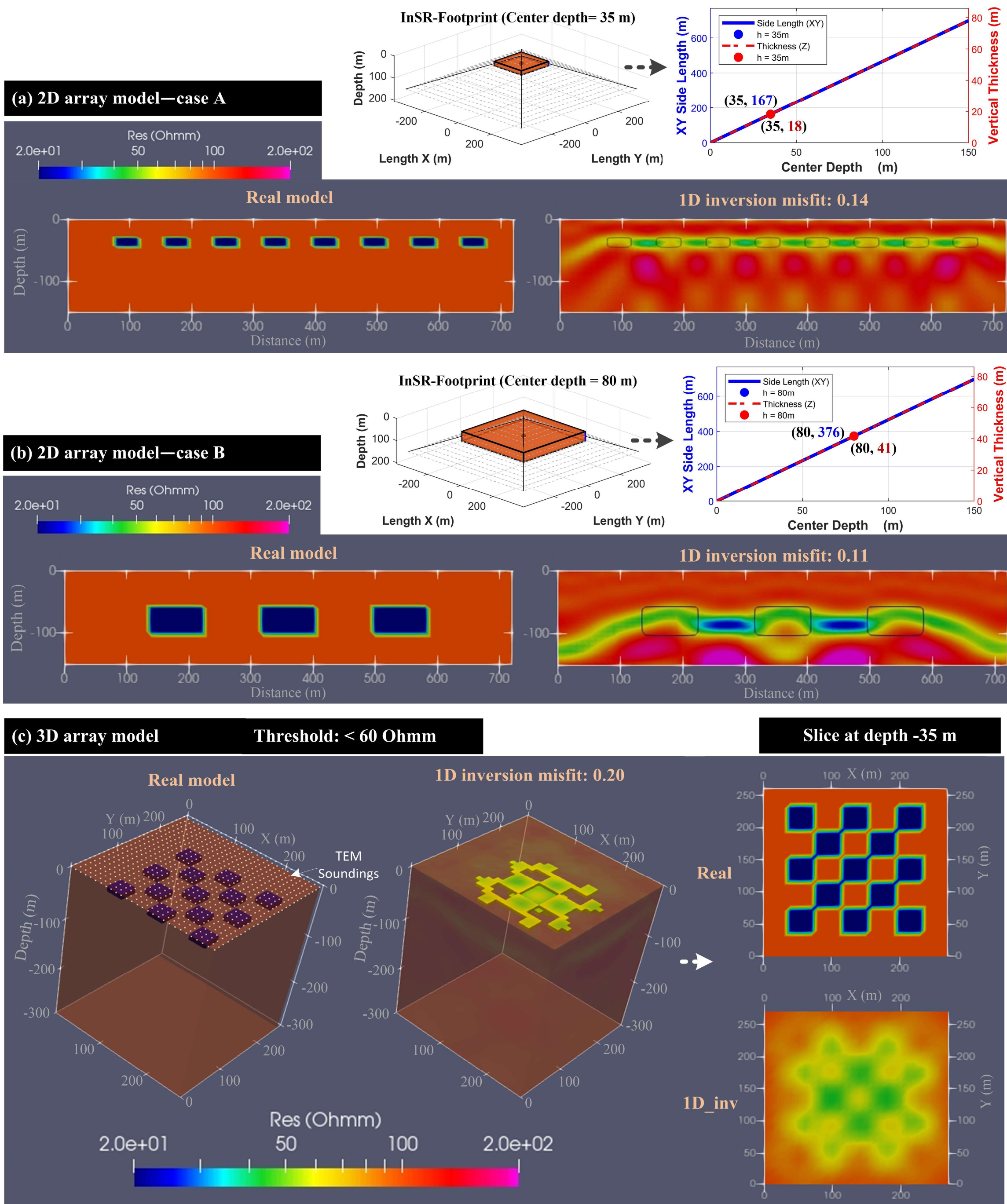

Figure 2. Conductive–resistive array models and their 1D inversion results. (a) A shallow 2D array model, representing a single row of alternating conductive bodies and resistive regions, with conductive bodies centred at ~35 m depth and spanning a depth interval of 30–42 m. (b) A deep 2D array model, with conductive bodies centred at ~80 m and spanning a depth interval of 60–100 m. (c) A 3D array model and its cross-sectional view, with conductive and resistive cells alternating in two horizontal directions. All forward simulations are based on tTEM system parameters. The 2D and 3D models employ both station and line spacings of 10 m. For all models, the background resistivity is 100 Ω·m, and the resistivity of the conductive anomalies is 20 Ω·m.

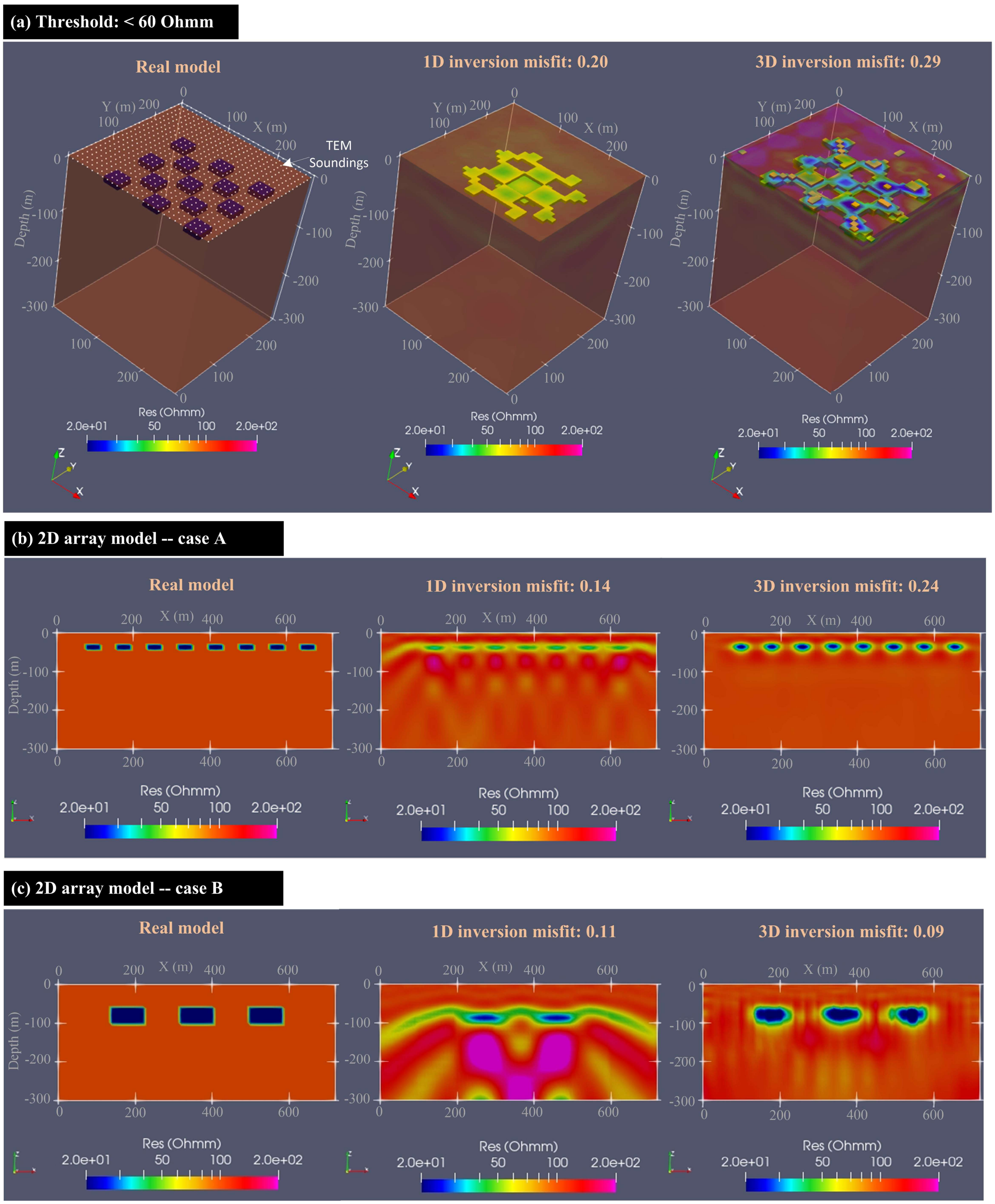

Figure 3. Conductive–resistive array models and their 3D inversion results. (a) 3D array model. (b) Shallow 2D array model with conductive bodies centred at ~35 m depth. (c) Deep 2D array model with conductive bodies centred at ~80 m depth.

It is well established that multidimensional structures can affect 1D inversion results; however, the extent to which array effects can cause such substantial lateral misplacement has not been widely recognized. The presence of array effects significantly distorts the spatial distribution of electrical anomalies in 1D inversion results, leading to potentially severe misinterpretations. Relying on these 1D inversion results for critical decision-making processes, such as borehole site selection, in areas where array effects are present could result in considerable potential losses. Moreover, the 1D inversion demonstrates good fitting accuracy to the observed data in both 2D and 3D models. This indicates that the occurrence of array effects is not controlled by the fitting ability of 1D inversion. Instead, 1D inversion can reproduce the data while assigning the response to incorrect lateral positions in the recovered model. It should be noted that array effects do not necessarily convert a conductive anomaly into a high-resistivity anomaly; rather, they distort the apparent lateral position of the strongest conductive response, thereby significantly misleading the 1D inversion results.

3. Field evidence from coastal airborne electromagnetic data

Array effects are not limited to synthetic models; here we examine a SkyTEM field example from a coastal dune area in the Netherlands. Figure 4(a) shows the SkyTEM airborne electromagnetic data collected in the study area. The survey area consists of five survey lines, each approximately 1.2 km long, with a spacing of about 200 m between lines and about 30 m between soundings. The average flight altitude of SkyTEM in this area is approximately 50 m. The survey area covers two freshwater lakes. As illustrated in Figure 4(b), all SkyTEM data were manually processed using the EEMstudio software platform (Sullivan et al., 2024) to remove data heavily contaminated by noise.

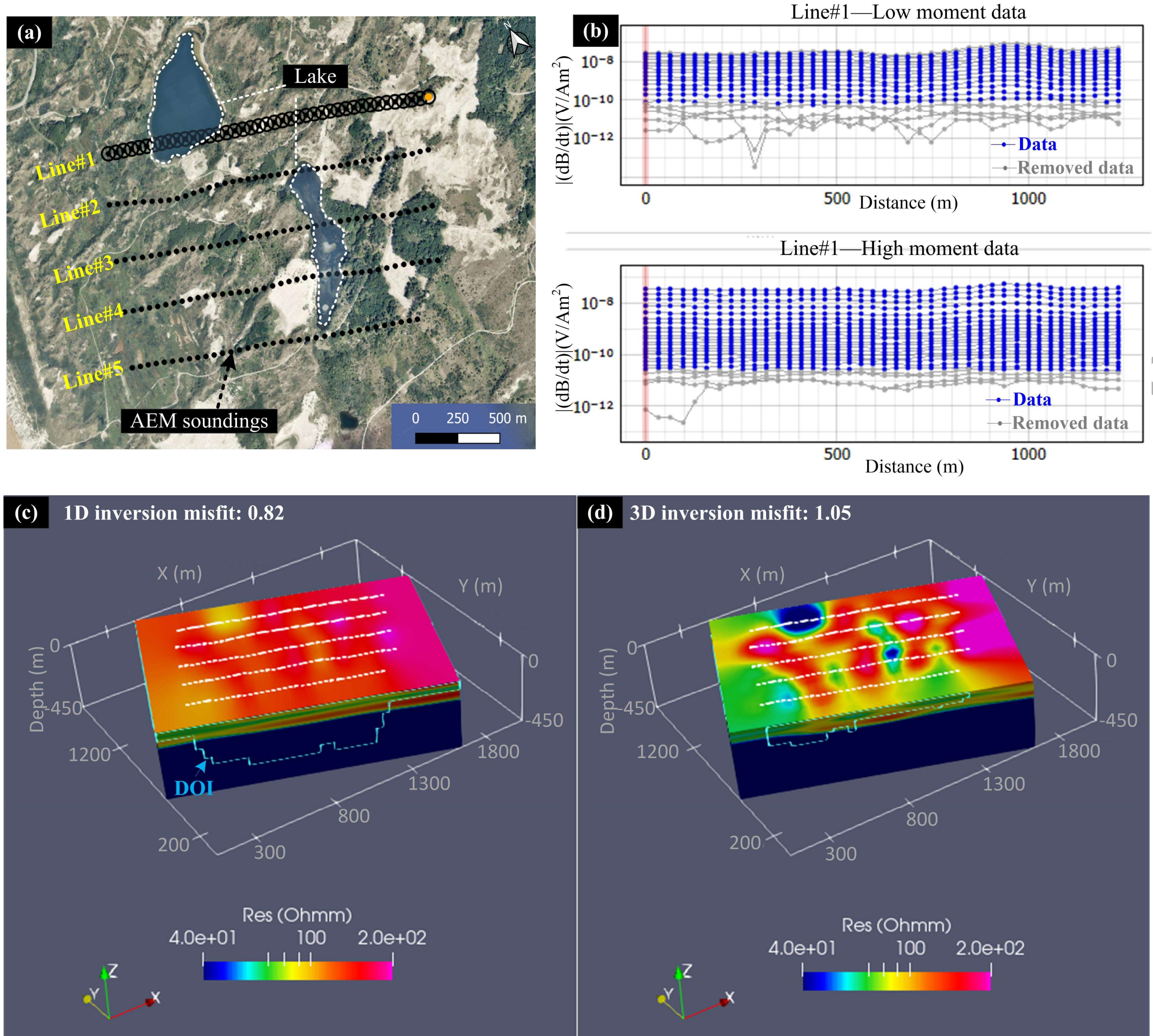

Figure 4. AEM data and inversion results in a coastal dune area of the Netherlands. (a) Map of SkyTEM survey lines along the dune area; (b) Display of data from the first survey line; (c) 1D inversion result; (d) 3D inversion result.

Figures 4(c) and 4(d) present a comparison of the inversion results using 1D and 3D operators, respectively, under the same model mesh. Visually, both inversion methods reveal resistivity differences near the surface freshwater lake, with the 3D inversion significantly enhancing the contrast of resistivity variations. In Figure 5, horizontal slices are shown at 38 m for the 1D model and 30 m for the 3D model, because the relatively conductive zones recovered by the two inversions occur at different apparent depths. Black dots on the 3D slice mark the horizontal extent of the relatively conductive zones recovered by the 1D inversion. These slices show strong lateral resistivity variations along the survey-line direction, consistent with a quasi-2D arrangement of conductive and resistive features. Because the 1D model between survey lines is interpolated from soundings along individual lines, our comparison focuses on the vertical sections directly beneath survey lines 2–4 in the central survey area. The figure focuses on the results within 100 m of the shallow subsurface; deeper regions, corresponding to seawater intrusion zones, fall outside the scope of this study.

In the 1D inversion results, relatively conductive zones are imaged at apparent depths of approximately 28–40 m. These zones are commonly located beneath shallow relatively resistive regions within the same 1D sections and show a discontinuous distribution along the survey lines. This spatial relationship is consistent with the misplacement pattern expected for array effects and is most pronounced along survey line 2, likely because this line crosses a broader zone of laterally alternating relatively conductive and resistive regions, as indicated by the horizontal slice. Along survey line 4, the conductive zone is mainly concentrated on the right side of the profile, and the corresponding misplacement pattern is also mainly observed on the right side.

Compared with the 1D results, the 3D inversion recovers the relatively conductive zones at slightly shallower apparent depths and, more importantly, at different lateral positions. This lateral mismatch suggests that the conductive features imaged by the 1D inversion are not simply the same anomalies recovered at a slightly different depth, but are likely artefacts associated with array effects. In other words, the 1D inversion appears to place relatively conductive anomalies beneath or near resistive intervals where the 3D inversion indicates a different lateral distribution of conductive material. This behaviour is consistent with the mechanism described in Section 2, in which laterally distributed conductive bodies and intervening resistive regions can lead to misplaced conductive anomalies in 1D inversion.

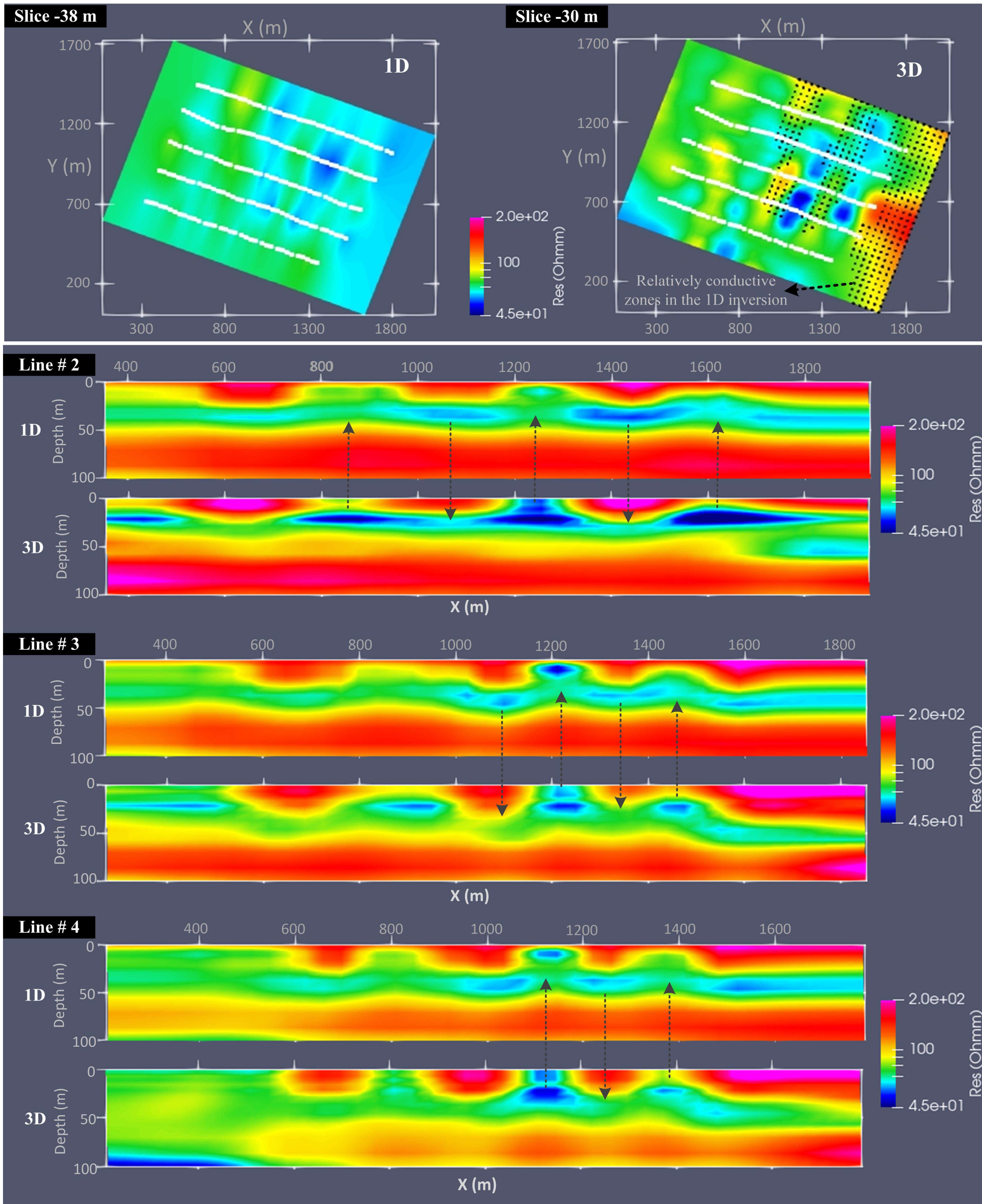

Figure 5. AEM 1D and 3D inversion results in the Dutch coastal dune area. The top row shows horizontal slices of the 1D model at 38 m and the 3D model at 30 m. Black dots on the 3D slice mark the horizontal extent of relatively conductive zones recovered by the 1D inversion, defined by resistivity $< 65\ \Omega\cdot\text{m}$. The lower rows show vertical sections beneath survey lines 2, 3, and 4; dashed arrows mark corresponding features between the 1D and 3D results.

The InSR-Footprint criterion provides an independent way to assess whether this interpretation is plausible. Using the empirical equations in Section 2.1, the horizontal length of the InSR-Footprint near the surface is approximately 210 m. In the upper 0–8 m, the conductive zones are not sufficiently clustered within the near-surface InSR-Footprint to couple multiple anomalies. This explains why array effects are not observed in this shallow interval. Instead, the smoother and wider conductive zones in the 1D inversion are more consistent with conventional 3D effects, where responses from laterally restricted conductors are averaged over a broader area and represented by the 1D inversion as wider anomalies. At an apparent depth of approximately 35–40 m, however, the horizontal length of the InSR-Footprint increases to more than 370 m. This range is large enough to include adjacent conductive zones separated by resistive regions, satisfying the condition for the conductive–resistive alternation mechanism. The contrast between the 1D and 3D inversion results at this depth is therefore consistent with the predicted array effects.

Additionally, both 1D and 3D methods can successfully fit the observed data, with misfits of 0.82 for the 1D method and 1.05 for the 3D method. This confirms that a low misfit in 1D inversion does not guarantee that the 1D approximation is valid or that the recovered model is geologically accurate.

4 Discussion

4.1 Impact of resistivity contrast on array effects

In this section, we investigate how conductor–background resistivity contrast influences array effects, using the shallow 2D conductive–resistive array model as a representative example. As illustrated in Figure 6(a), forward modelling was conducted using tTEM system parameters, with the model geometry consistent with that in Figure 2(a). For the baseline simulation, the conductor and background resistivities were set to 20 Ω·m and 100 Ω·m, respectively. Building on this, we further examined scenarios where the background resistivity was increased to 500 Ω·m and 2000 Ω·m. Additionally, to explore scenarios with higher target conductivity, we set the conductor resistivity to 2 Ω·m and evaluated 1D inversion results with background resistivities of 10, 50, and 200 Ω·m.

Figures 6(a)–6(c) show that, for the 20 Ω·m conductor, the characteristic lateral misplacement persists as the background resistivity increases. At a contrast ratio of 100, the misplaced conductive anomalies become more vertically extended and appear at greater apparent depths. Pant-leg-like artefacts also become more pronounced near the margins of the conductor array. This is likely because induced currents diffuse more rapidly in a more resistive background, increasing the lateral diffusion range at a given time and allowing soundings near the array edges to receive stronger contributions from laterally offset conductors. Because 1D inversion cannot represent the lateral origin of these responses, it maps them beneath the sounding locations, producing downward-extended conductive artefacts on the flanks.

For the 2 Ω·m conductor cases [Figures 6(d)–6(f)], array effects remain evident at low resistivity contrast. As the contrast ratio increases to 25, the misplacement pattern remains observable; however, the spurious artefacts begin to migrate deeper, while the true conductors begin to be partially resolved in the inversion. When the contrast ratio reaches 100, the true conductors and spurious artefacts begin to coalesce into a single connected feature, with the artefacts appearing slightly deeper and thicker. In addition, under this high-contrast condition, several conductive anomalies appear at a depth of approximately 130 m in the central region. We interpret these anomalies as resulting from the superposition of responses from adjacent conductors, which increases the late-time response. To fit this excess late-time signal within a 1D parameterisation, the inversion introduces secondary deep conductive artefacts beneath the central part of the conductor array.

In summary, array effects retain their characteristic lateral misplacement pattern under moderate resistivity contrasts. However, with increasing resistivity contrast, the interaction between strong electrical contrast and lateral geometric effects further exacerbates the distortion, producing more severe artefacts in the 1D inversion results.

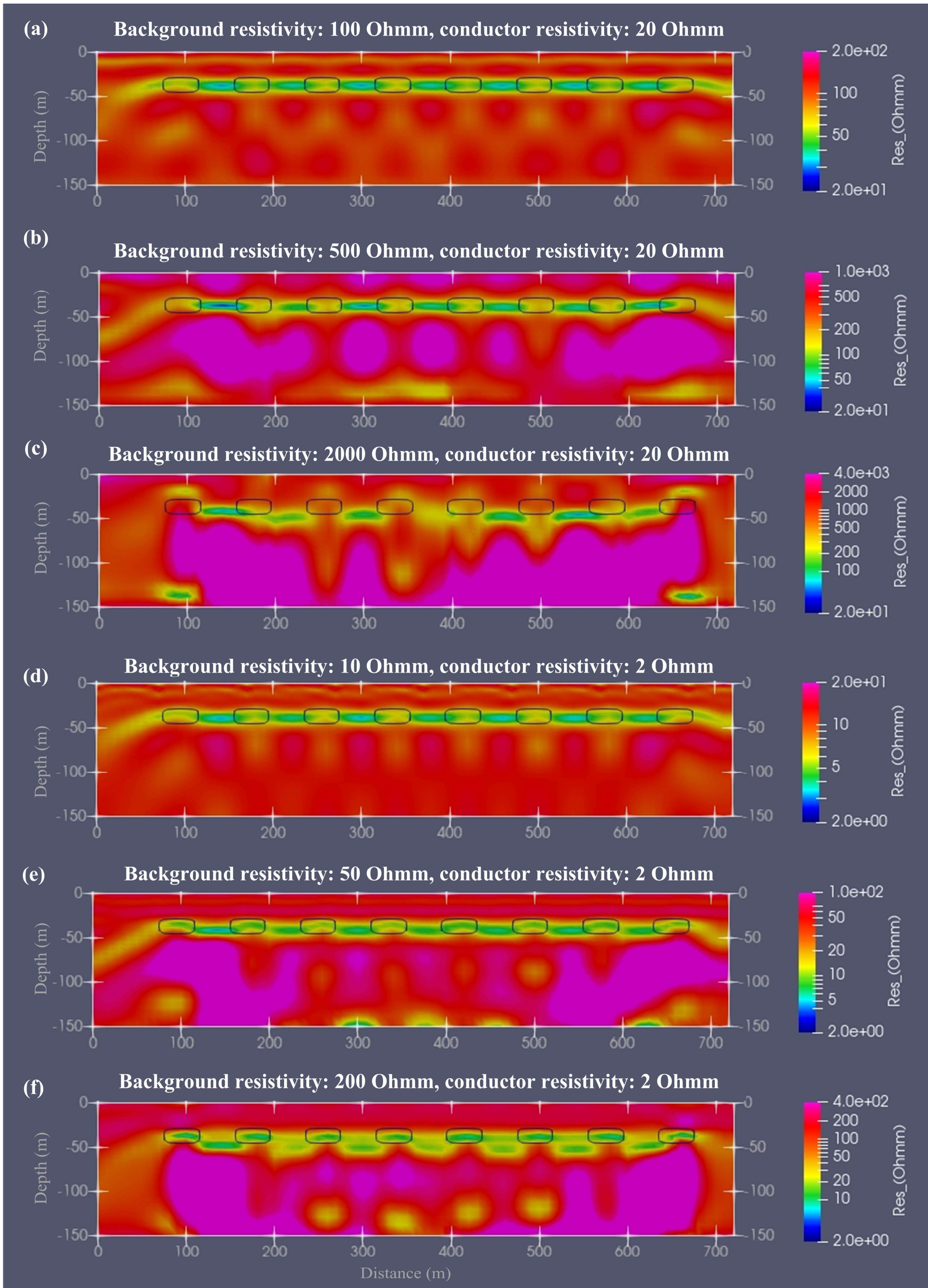

Figure 6. Effect of conductor–background resistivity contrast on the 1D inversion of the 2D conductive–resistive array model. Panels (a)–(c) and (d)–(f) show inversion results for conductor resistivities of 20 Ω·m and 2 Ω·m, respectively, with resistivity contrast ratios of 5, 25, and 100. All simulations use tTEM system parameters with a sounding spacing of 10 m. The black rectangles indicate the locations of the true conductors.

4.2 Impact of flight height, conductor spacing, and burial depth on array effects

While the previous sections focused on ground-based systems, this section uses the SkyTEM system as a representative AEM configuration to investigate the influence of flight height, conductor spacing, and burial depth on array effects. As illustrated in Figure 7(a), and following the design principles outlined in Section 2, we constructed a standard 2D conductive–resistive array model with a reference flight height of 40 m. The model consists of two identical conductors, each 80 m wide and 12 m thick, with their centres located at a depth of 35 m and separated by an 80 m resistive gap.

We first examine the impact of flight height, which strongly controls the spatial dimensions of the InSR-Footprint. For the hypothetical ground-based case ($h = 0$ m), the horizontal length of the InSR-Footprint at the 35 m conductor-centre depth is approximately 167 m. When the sounding location is midway between the two conductors, this footprint only partially covers the conductive bodies. Consequently, the response in the resistive gap is expected to be lower than that directly above the conductors. For an AEM flight height of 80 m, however, the InSR-Footprint expands to approximately 500 m. In this case, the footprint is large enough to include both conductors simultaneously, so a strong response can still be observed above the central gap. Compared with lower altitudes, higher flight heights increase the InSR-Footprint and cause the pant-leg-like artefacts flanking the conductors to extend farther laterally.

Figures 7(b)–7(d) show the 1D inversion results for flight heights of 0 m, 40 m, and 80 m, respectively. Although the 0 m case is operationally unrealistic for AEM, it is included as a baseline control model. The results at different flight heights are broadly consistent with the predictions of the InSR-Footprint theory, with array effects appearing at different levels of intensity. In the 0 m case, the response in the central resistive gap is weaker than that directly above the conductors, so the two conductors remain distinguishable in the 1D inversion. However, the inversion also generates a deeper spurious conductive anomaly within this gap. This anomaly can be interpreted as the intersection at depth of pant-leg-like artefacts from the adjacent conductors.

Next, we investigate the influence of conductor spacing. When the spacing is reduced relative to the standard 2D array model, the responses associated with adjacent conductors overlap more strongly across the intervening resistive gap. As a result, the two separate conductors may appear in the 1D inversion as a single, laterally connected conductive feature. Conversely, when the spacing is large relative to the InSR-Footprint, the two conductors are sensed more independently and are therefore imaged as distinct features. Figures 7(e) and 7(f) present the 1D inversion results for the narrow- and wide-spacing models, respectively, showing good agreement with this interpretation.

Finally, we examine the influence of burial depth. Figures 7(g) and 7(h) show that, for deeply buried conductors, the enlarged InSR-Footprint causes the adjacent conductors and the intervening resistive gap to be sensed together, resulting in a broad deep conductive anomaly in the 1D inversion. In this case, the separation between the conductors becomes indistinguishable. For shallowly buried conductors, the 40 m flight height still produces a relatively large near-surface InSR-Footprint, with a horizontal length of approximately 168 m. This configuration is similar to the case in Figure 7(c): the 1D inversion partly resolves the two conductors, but also generates a deeper spurious conductive anomaly between them.

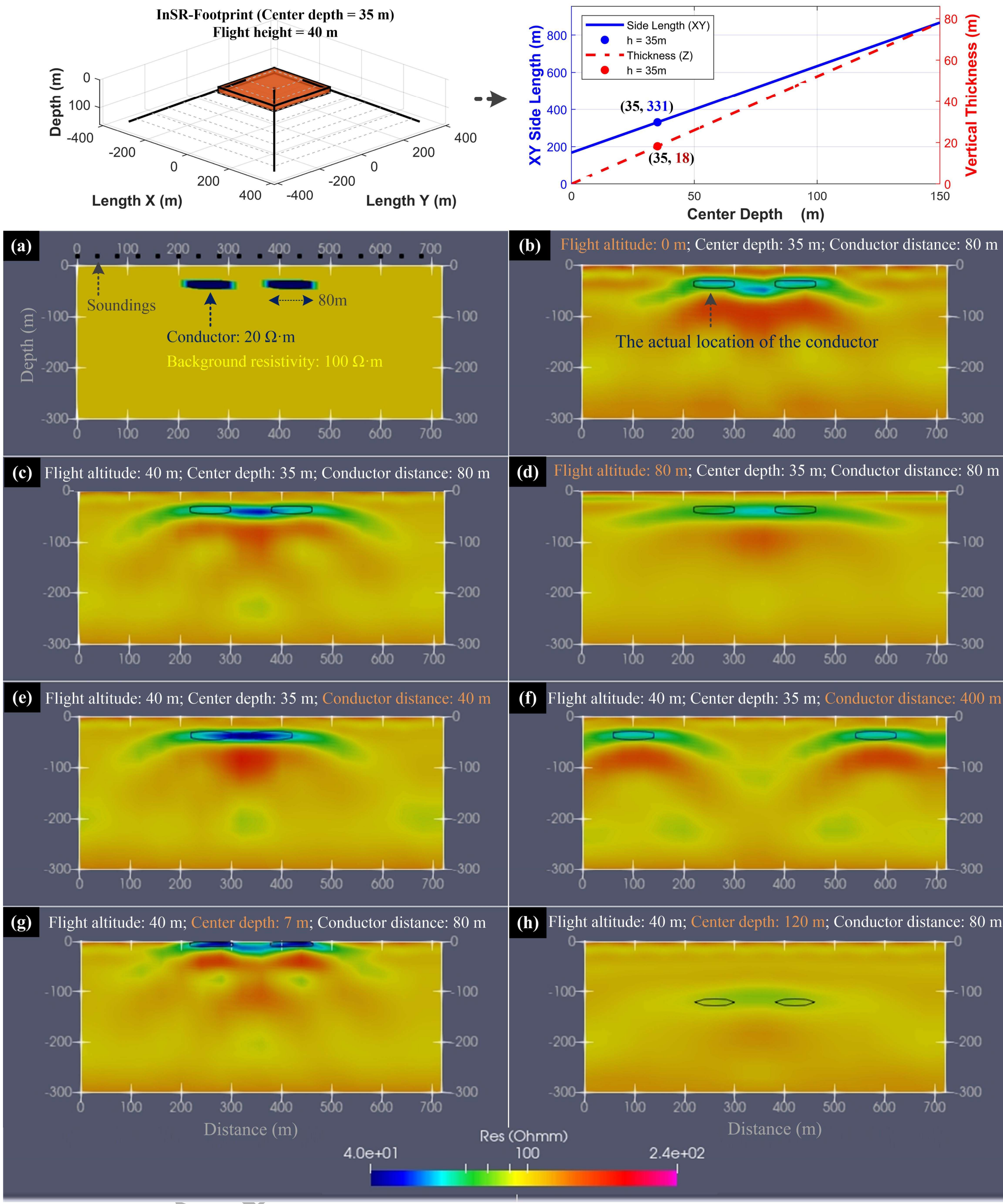

Figure 7. 2D conductive–resistive array models simulated using SkyTEM system parameters and their 1D inversion results. The upper panels show the calculated AEM InSR-Footprint and its XY side length and vertical thickness as functions of target centre depth. (a) Standard 2D array model designed according to the InSR-Footprint criterion; (b) zero flight altitude; (c) inversion results of the standard 2D array model; (d) flight altitude set to 80 m; (e) conductor spacing set to 40 m; (f) conductor spacing set to 400 m; (g) centre depth set to 7 m; (h) centre depth set to 120 m. The spacing between the AEM soundings is 40 m. All conductors are 12 m thick and 80 m long.

5 Conclusions

In this study, we identify and analyse array effects in TEM/AEM 1D inversion. These effects occur when multiple conductive bodies and intervening resistive regions fall within the instantaneous influence region of the TEM response. In this case, the strongest induced response may deviate from, or even shift away from, the area directly above the true conductors. As a result, 1D inversion may place conductive anomalies into, or towards, intervening resistive regions, resulting in laterally misplaced anomalies. The underlying physical cause is the conductive–resistive alternation mechanism.

Compared with conventional multidimensional effects, array effects can have a more severe impact on 1D inversion because they may not only distort the shape of conductive anomalies but also misplace their apparent lateral positions. To analyse and identify this behaviour, we use the InSR-Footprint based on smoke-ring theory, which provides a practical criterion for estimating whether adjacent conductive bodies and intervening resistive regions are likely to be coupled within the TEM response region. Synthetic modelling results show that both 2D and 3D conductive–resistive array models can produce this type of misplacement in 1D inversion. In the shallow and deep 2D array models, 1D inversion places conductive anomalies within or towards resistive regions, whereas 3D inversion recovers the true conductor positions much more accurately. The 3D array model demonstrates that the same conductive–resistive alternation mechanism can also operate when conductive and resistive regions vary in two horizontal directions.

The field example from the Dutch coastal dune area, based on SkyTEM data, provides supporting evidence for array effects in real AEM data. In the 1D inversion results, relatively conductive zones are imaged beneath or near resistive intervals, whereas the 3D inversion places the corresponding conductive regions at different lateral positions. This behaviour is consistent with the conductive–resistive alternation mechanism and with the InSR-Footprint criterion.

Further numerical experiments indicate that flight height, conductor spacing, burial depth, resistivity contrast, and background resistivity influence the strength and expression of array effects. Under moderate resistivity contrasts, the characteristic lateral misplacement pattern remains broadly consistent with the InSR-Footprint prediction. At higher contrasts, the interaction between strong electrical contrast and lateral geometric effects can produce deeper and more complex artefacts in the 1D inversion results.

The conductive–resistive alternation mechanism is not limited to the idealized 2D and 3D array models examined here. Related misplacement may also occur in other configurations where conductive material within the effective TEM response region dominates the measured signal and is projected by 1D inversion into intervening or enclosed resistive regions. For example, the Mt. Milligan-style structure discussed by Yang and Oldenburg (2012) represents a different geometry, but reflects a related physical mechanism.

Finally, our results show that a low data misfit from 1D inversion does not guarantee that the 1D approximation is valid or that the recovered model is geologically accurate. Therefore, in areas where multiple conductive and resistive features may be coupled within the same InSR-Footprint, 1D inversion results should be interpreted with caution. In such cases, 3D modelling or inversion is essential for reliable anomaly mapping and geological interpretation.

Acknowledgments

This study has been carried out within the Horizon Europe project SEMACRET (Grant Agreement no. 101057741). It was also funded under the 'Progetto di Eccellenza 2023–2027: Le Georisorse per la Transizione Ecologica e lo Sviluppo Territoriale' by the Italian Ministry of University and Research. The authors acknowledge support from the University of Milan through the APC initiative. The authors are grateful to Andrea Viezzoli for the helpful discussions. We also thank James Macnae and Leif Cox for their constructive reviews and insightful suggestions, which helped improve the clarity and rigor of the manuscript. The authors declare that there are no conflicts of interest.

Data Availability Statement

The airborne electromagnetic data used in this study are available at https://doi.org/10.13130/RD_UNIMI/SK4K2K (Chen et al., 2026b).

References

Auken, E., Christiansen, A. V., Jacobsen, L. H., Sørensen, K. I. (2008). A resolution study of buried valleys using laterally constrained inversion of TEM data. *Journal of Applied Geophysics*, *65(1)*, 10–20. https://doi.org/10.1016/j.jappgeo.2008.03.003.

Auken, E., Foged, N., Larsen, J. J., Lassen, K. V. T., Maurya, P. K., Dath, S. M., & Eiskjær, T. T. (2019). tTEM — A towed transient electromagnetic system for detailed 3D imaging of the top 70 m of the subsurface. *Geophysics*, *84*(1), E13–E22. https://doi.org/10.1190/GEO2018-0355.1.

Chandra, S., Tiwari, V. M., Vidyasagar, M., Raju, K. B., Choudhury, J., Lohithkumar, K., et al. (2021). Airborne electromagnetic signatures of an ancient river in the water-stressed Ganga Plain, Prayagraj, India: A potential groundwater Repository. *Geophysical Research Letters*, *48*, e2021GL096100. https://doi.org/10.1029/2021GL096100.

Chen, J., Zhang, Y., & Lin, T. (2023). High-resolution quasi-three-dimensional transient electromagnetic imaging method for urban underground space detection. *IEEE Transactions on Industrial Informatics, 19(3)*, 3039–3046. https://doi.org/10.1109/TII.2022.3176890.

Chen, J., Dauti, F., Wertich, V., Viezzoli, A., Zhang, B., & Fiandaca, G. (2026a). 3D EM inversion considering induced polarization effect. *Geophys. J. Int.,* https://doi.org/10.1093/gji/ggaf462.

Chen, J., Galli, S., Signora, A., Sullivan, N. A. L., Zhang, B., & Fiandaca, G. (2025). Rapid Bayesian Imaging of Large-Scale Transient Electromagnetic Data Using Probabilistic Neural Networks. *Journal of Geophysical Research: Machine Learning and Computation*, *2*(2), e2024JH000536.

Chen, J., Schaars, F., Fiandaca, G. (2026b). SkyTEM survey in dune area. *UNIMI Dataverse*. https://doi.org/10.13130/RD_UNIMI/SK4K2K.

Commer, M., and Newman, G. (2004). A parallel finite-difference approach for 3D transient electromagnetic modeling with galvanic sources. *Geophysics*, *69*(5), 1192–1202.

Cox, L.H., Wilson, G.A., and Zhdanov, M.S. (2010). 3D inversion of airborne electromagnetic data using a moving footprint. *Exploration Geophysics*, 41, 250–259.

Cox, L. H., Wilson, G. A., & Zhdanov, M. S. (2012). 3D inversion of airborne electromagnetic data. *Geophysics*, *77*(4), WB59-WB69. https://doi.org/10.1190/geo2011-0370.1.

Cox, L.H., Zhdanov, M. S. & Prikhodko, A., 2024. Inversion for 3D Conductivity and Chargeability Models Using EM Data Acquired by the New Airborne TargetEM System in Ontario, Canada, *Minerals*, 14(237).

Ellis, R.G. (1998). Inversion of airborne electromagnetic data. *Exploration Geophysics*, *29*, 121–127.

Fiandaca, G., Chen J., & Zhang, B., 2024. EEMverter, a New Modelling Tool for Electric and Electromagnetic Data with Focus on Induced Polarization, European Association of Geoscientists & Engineers, NSG 2024 30th European Meeting of Environmental and Engineering Geophysics, Sep 2024, 1–5, https://doi.org/10.3997/2214-4609.202420166.

González-Álvarez, I., Ley-Cooper, A.-Y., Salama, W. (2015). A geological assessment of airborne electromagnetics for mineral exploration through deeply weathered profiles in the southeast yilgarn cratonic margin, Western Australia. *Ore Geology Reviews*. https://doi.org/10.1016/j.oregeorev.2015.10.029.

Haber, E., Oldenburg, D.W., and Shekhtman, R. (2007). Inversion of time domain three-dimensional electromagnetic data. *Geophysical Journal International, 171*, 550–564.

Heagy, L.J., Oldenburg, D.W., Kang, S., and Yang, D. (2025). Why every electromagnetic inversion needs a 3D forward simulation. The Leading Edge, 44(11), 847–854. https://doi.org/10.1190/tle44110847.1.

Haber, E., and Schwarzbach, C. (2014). Parallel inversion of large-scale airborne time-domain electromagnetic data with multiple OcTree meshes. *Inverse Problems*, 30. https://doi.org/10.1088/0266-5611/30/5/055011.

Hoversten, G. M., & Morrison, H. F. (1982). Transient fields of a current loop source above a layered earth. *Geophysics*, *47*(7), 1068-1077.

Lane, R., Green, A., Golding, C., Owers, M., Pik, P., Plunkett, C., Sattel, D., & Thorn, B. (2000). An example of 3D conductivity mapping using the TEMPEST airborne electromagnetic system. *Exploration Geophysics*, *31*(1-2), 162-172.

Lane Jr., J.W., Briggs, M.A., Maurya, P.K., White, E.A., Pedersen, J.B., Auken, E., Terry, N., Minsley, B., Kress, W., LeBlanc, D.R., Adams, R., and Johnson, C.D. (2020). Characterizing the diverse hydrogeology underlying rivers and estuaries using new floating transient electromagnetic methodology. *Science of The Total Environment*, *740*, https://doi.org/10.1016/j.scitotenv.2020.140074.

Ley-Cooper, A.Y., Macnae, J., and Viezzoli, A. (2010). Breaks in lithology: Interpretation problems when handling 2D structures with a 1D approximation. *Geophysics*, 75(4), 179–188.

Lin, J., Chen, J., & Zhang, Y. (2021). Rapid and high-resolution detection of urban underground space using transient electromagnetic method. *IEEE Transactions on Industrial Informatics*, *18*(4), 2622-2631.

Liu, G., and Becker, A. (1990). Two-dimensional mapping of sea-ice keels with airborne electromagnetics. *Geophysics*, 55(2), 239–248.

Macnae, J., & Hine, K. (2025). Correcting low-frequency EM data using inverted IP parameters of regolith clays. Geophysical Journal International, 243, 1–11. https://doi.org/10.1093/gji/ggaf367.

Moon, C. J. (2010). Geochemical exploration in Cornwall and Devon: a review. Geochemistry: Exploration, Environment, Analysis, 10(3), 331–351. https://doi.org/10.1144/1467-7873/09-239.

Nabighian, M. (1979). Quasi-static transient response of a conducting half-space — An approximate representation. *Geophysics*, 44(10), 1700–1705.

Oldenburg, D.W., Heagy, L.J., Kang, S., & Cockett, R. (2019). 3D electromagnetic modelling and inversion: a case for open source. *Exploration Geophysics*, https://doi.org/10.1080/08123985.2019.1580118.

Oristaglio, M. L., & Hohmann, G. W. (1984). Diffusion of electromagnetic fields into a two-dimensional earth: A finite-difference approach. *Geophysics*, *49*(7), 870–894. https://doi.org/10.1190/1.1441733.

Paterson, R. (2020). 2.5D Airborne Electromagnetic inversion: A review of the benefits of moving to a higher dimension. Preview, 207, 33–47. https://doi.org/10.1080/14432471.2020.1801314.

Sørensen K.I. and Auken E. (2004). SkyTEM—A new high-resolution helicopter transient electromagnetic system. *Exploration Geophysics, 35*, 191–199.

Silvestri, S., Christensen, C. W., Lysdahl, A. O. K., Anschütz, H., Pfaffhuber, A. A., & Viezzoli, A. (2019). Peatland volume mapping over resistive substrates with airborne electromagnetic technology. *Geophysical Research Letters*, *46*, 6459–6468. https://doi.org/10.1029/2019GL083025.

Silic, J., Paterson, R., & FitzGerald, D. (2018). 2.5 D vs 1D AEM Forward and Inversion Methods at a Survey Scale: A Case Study. *ASEG Extended Abstracts*, *2018*(1), 1-8. https://doi.org/10.1071/ASEG2018abM2_1E.

Sullivan, N. A. L., Viezzoli, A., & Fiandaca, G. (2024). EEMstudio: Process and model electric and electromagnetic data with a QGIS plugin. In *NSG 2024 30th European Meeting of Environmental and Engineering Geophysics* (Vol. 2024, pp. 1–5). European Association of Geoscientists & Engineers. https://doi.org/10.3997/2214-4609.202420154.

Viezzoli, A., Tosi, L., Teatini, P., and Silvestri, S. (2010). Surface water – groundwater exchange in transitional coastal environments by airborne electromagnetics: The Venice Lagoon example. *Geophysical Research Letters*, *37*, L01402. https://doi.org/10.1029/2009GL041572.

Vignoli, G., Fiandaca, G., Christiansen, A.V., Kirkegaard, C. and Auken, E. (2015). Sharp spatially constrained inversion with applications to transient electromagnetic data. *Geophysical Prospecting, 63*, 243–255. https://doi.org/10.1111/1365-2478.12185.

Viezzoli, A., Christiansen, A., Sorensen, K., and Auken, E. (2008). Quasi-3D modeling of airborne TEM data by spatially constrained inversion. *Geophysics*, *73*(3).

Ward, S.H., & Hohmann, G.W. (1988). Electromagnetic theory for geophysical applications. In M. N. Nabighian (Ed.), *Electromagnetic Methods in Applied Geophysics, Vol. 1: Theory* (pp. 131–311). Society of Exploration Geophysicists.

Witherly, K., Irvine, R., & Morrison, E. B. (2004). The Geotech VTEM time domain helicopter EM system. *ASEG Extended Abstracts*, *2004*(1), 1-4.

Yin, C.C., Qi, Y.F., Liu, Y. H., and Cai, J. (2016). 3D time-domain airborne EM forward modeling with topography. *Journal of Applied Geophysics*, *134*, 11–22.

Yang, D., Oldenburg, D.W., and Haber, E. (2014). 3-D inversion of airborne electromagnetic data parallelized and accelerated by local mesh and adaptive soundings. *Geophysical Journal International,* 196, 1492–1507.

Yang, D., and Oldenburg, D.W. (2012). Three-dimensional inversion of airborne time-domain electromagnetic data with applications to a porphyry deposit. *Geophysics,* 77(2), 23–34.

Zhang, B., Yin, C. C., Liu, Y. H., Ren, X. Y., Baranwal, V. C. and Xiong, B., 2021. 3D inversion of large-scale frequency-domain airborne electromagnetic data using unstructured local mesh. *Geophysics*, 86(5), 333-342.

Zhdanov, M. S., Gribenko, A., Cox, L., Tanabe, K., Hato, T., & Tsukamoto, A. (2025). Modelling and inversion of superconducting quantum interference device transient electromagnetic survey data for geothermal resource exploration. *First Break*, *43*(9), 37–42. https://doi.org/10.3997/1365-2397.fb2025066.